High-Resolution Detection of Periglacial Landforms Deformation Using Radarsat-2 and GF-7 Stereo Optical Imagery

Xuefei Zhang ⓘ, Min Feng ⓘ, Tao Li ⓘ, Jiyi Chen ⓘ, Decai Jiang, Jinhao Xu, Dezhao Yan, Xiaoqing Zhou, Xiang Zhang, and Jing Lu ⓘ

Abstract—In cold mountain environments, rock glaciers and talus represent common periglacial landforms. Accurate monitoring of their activity is crucial for understanding alpine kinematics. Presently, spaceborne SAR satellites monitor periglacial landform deformations mainly utilizing medium-resolution data. However, capturing surface structure deformations accurately and comprehending the movement mechanisms remain challenging. This study employs high-resolution GF-7 optical stereo images and Radarsat-2 SAR data, introducing a multibaseline persistent scatterer and distributed scatterer combined multitemporal InSAR (MT-InSAR) method to identify rock glaciers and talus landforms, as well as to analyze their deformations. Initially, rock glaciers and talus are outlined using GF-7 optical images, and digital surface models are extracted. The developed MT-InSAR method then detects the line of sight and slope-parallel deformations of these landforms. Radarsat-2 monitoring reveals that 47.5% of identified rock glaciers are classified as active, while talus deformations are less active compared to rock glaciers. By utilizing high-resolution optical and SAR satellite data, we first documented the intricate deformation features within standard rock glaciers, such as the front, lateral margins, and optionally ridge-and-furrow deformations, as well as their interaction with the surrounding terrain topography. This discovery offers evidence of gravity-driven forces impacting rock glacier movement. We have also conducted a deformation analysis of the talus, obtaining spatial deformation characteristics of typical talus. It was observed that the deformation of the talus is jointly influenced by the conditions of surface debris cover and the slope of the terrain. This study highlights the value of high-resolution optical and SAR satellites in studying periglacial geomorphology dynamics.

Index Terms—Deformation, multitemporal InSAR (MT-InSAR), periglacial landforms, rock glacier, talus.

I. INTRODUCTION

ROCK glaciers are typical periglacial landforms that develop widely in alpine mountain permafrost environments [1], [2], [3]. As the periglacial landscape evolves, the ice content beneath the debris cover gradually decreases, transitioning from massive sediments to soil matrix ice lenses. Rock glaciers and talus play vital roles in this continuous periglacial landform evolution process, often forming part of the sequence ice cirque-debris-covered rock glacier-talus [4]. Both rock glaciers and talus exhibit common creeping and rheological properties [2], [5]. The transportation of debris and moraine is a significant source of landslides, posing potential threats to infrastructure and development [6], [7]. In the context of climate change, some periglacial environments have seen accelerated surface movement in rock glaciers due to permafrost warming, increased water access to deeper permafrost layers, and internal shear zones [8]. Monitoring the temporal-spatial deformation of rock glaciers and talus can enhance our understanding of how climate and hydrological variables may impact the evolution of periglacial environments [9], [10], [11].

Traditional monitoring of surface deformation in periglacial landforms primarily relies on ground-based equipment such as GNSS, LiDAR, GPS, and ground-based interferometric synthetic aperture radar [12], [13], [14]. However, in recent years, remote sensing techniques such as aerial photogrammetry, high-resolution optical satellite imagery, unmanned aerial vehicles, and airborne laser scanning have gained broader usage [15], [16], [17], [18]. Nonetheless, rock glaciers and talus are typically found in remote, high-altitude, and challenging environments. This makes traditional monitoring methods expensive, limited in their coverage, and challenging to implement widely. Additionally, optical satellite data can be affected by cloud cover and fog, limiting observational accuracy [11], [19].

The continual expansion of spaceborne synthetic aperture radar (SAR) data and the rapid development of interferometric

Xuefei Zhang, Tao Li, Jiyi Chen, Xiaoqing Zhou, Xiang Zhang, and Jing Lu are with the Land Satellite Remote Sensing Application Center, Ministry of Natural Resources, Beijing 100048, China (e-mail: zhangxf@lasac.cn; rs_litao@163.com; chenjy@lasac.cn; zhouxq@lasac.cn; zhangx@lasac.cn; luj@lasac.cn).

Min Feng is with the National Tibetan Plateau Data Center, State Key Laboratory of Tibetan Plateau Earth System, Environment and Resources, Institute of Tibetan Plateau Research, Chinese Academy of Sciences, Beijing 100045, China, and also with the Academy of Plateau Science and Sustainability, Qinghai Normal University, Xining 810008, China (e-mail: mfeng@itpcas.ac.cn).

Decai Jiang, Jinhao Xu, and Dezhao Yan are with the National Tibetan Plateau Data Center, State Key Laboratory of Tibetan Plateau Earth System, Environment and Resources, Institute of Tibetan Plateau Research, Chinese Academy of Sciences, Beijing 100045, China (e-mail: jiangdc_rs@126.com; xujinhao@itpcas.ac.cn; yandezhao@itpcas.ac.cn).

Digital Object Identifier 10.1109/JSTARS.2024.3407791

SAR (InSAR) and multitemporal InSAR (MT-InSAR) technology have enabled multiscale and continuous monitoring of periglacial landform movements in various cryospheric environments [20], [21], [22], [23], [24], [25], [26], [27], [28]. Some regions have successfully created inventories of rock glaciers that include standard activity attributes, following the guidelines established by the International Permafrost Association (IPA) [29], [30]. This has significantly improved our comprehension of rock glacier activity [24], [26], [28], [31], [32].

Currently, surface deformation monitoring and activity detection of rock glaciers using InSAR technology mostly revolve around short-term and medium-resolution observations, often with data from Sentinel-1, and ALOS-1 PALSAR, among others [24], [33]. Those data may fail to accurately capture deformation variations in rock glacier surface structure, especially in the case of small rock glaciers. Consequently, significant knowledge gaps persist regarding the spatiotemporal motion mechanisms of rock glaciers.

Presently, research on talus primarily emphasizes morphological characteristics, sediment thickness measurement, and geophysical investigations, such as rock weathering [2]. However, examining the kinematics of talus geomorphology is crucial for enhancing our understanding of periglacial talus formation, evolution, and the broader periglacial landscape. The movement of talus directly reflects the geomorphic evolution and serves as a crucial basis for preventing rockfall disasters in mountainous areas. The main reasons for the movement of debris on talus slopes include rockfalls, freeze-thaw action, water flow, avalanches, and other factors [34], [35]. In a limited number of studies, Imaizumi et al. [36] used InSAR technology with three-scene PALSAR data to analyze the deformation characteristics of 38 rockfall slopes in various terrains in the southern Swiss Alps [36]. Dini et al. [37] determined the deformation rates of certain talus formations in the northwest Himalayan Mountains of Bhutan from 2007 to 2010 using SBAS technology. There is a shortage of research on talus movement using InSAR technology [38]. The potential of InSAR for inventorying talus landforms and contributing to geomorphological studies in complex periglacial environments requires further exploration.

On the other hand, the use of MT-InSAR for estimating deformations in periglacial landforms is also affected by factors such as tropospheric atmospheric delay, arising from the significant variations in relief elevation in periglacial environments, phase unwrapping errors due to complex terrain, and interferometric decorrelation caused by snowmelt [28], [32], [38], [39]. Further research is needed to explore the application of the MT-InSAR method with high-resolution SAR data to periglacial landforms.

In this article, we present a multibaseline PS-DS combined MT-InSAR network designed to obtain comprehensive and detailed deformation measurements of periglacial landforms in the Eastern Himalayas, with a focus on rock glaciers and talus, using high-resolution Radarsat-2 and GF-7 optical stereo images. To illustrate the advantages of our high-resolution deformation monitoring, we compare the results with those obtained from Radarsat-2 and Sentinel-1 data. We classify the activity of rock glaciers and talus in Southeast the Himalayas and analyze the spatial characteristics of surface deformation in typical active rock glaciers and talus.

II. STUDY AREA AND DATASET

A. Study Area

The study area, located near Gangkhar Puensum in the southeast Himalayas, is characterized by extreme environmental and climatic conditions, intricate terrain, and a substantial altitude variation of over 6000 m (Fig. 1). Rock glaciers and talus are prevalent throughout this region [Fig. 1(e)]. Utilizing high-resolution optical remote sensing images from GF-7 with a 1-m resolution [Fig. 1(d)], which combines panchromatic and multispectral data, we have successfully identified rock glaciers and talus [Fig. 1(e)].

B. GF-7 Data

GF-7 is China's inaugural civil optical stereo mapping satellite, boasting a submeter resolution, and it was launched in November 2019. It can efficiently capture front-view and rear-view panchromatic stereoscopic images using a dual-line-array camera, as well as multispectral images with a laser altimeter system, offering resolutions of 0.8 m, 0.65 m, and 2.6 m, respectively. In our research, we procured five scenes of GF-7 stereo and multispectral optical images that had minimal cloud cover. Additionally, laser altimetry data were obtained to generate high-resolution digital surface models (DSMs) [Fig. 1(b) and (c)] and delineate the outlines of rock glaciers and talus in our study area [Fig. 1(d) and (e)]. The GF-7 data can be accessed via the Natural Resources Satellite Remote Sensing Cloud Service Platform (http://sasclouds.com/english/home) and were acquired from the Land Satellite Remote Sensing Application Center (LASAC). Specific details regarding these GF-7 stereo images can be found in Table I.

C. SAR Data

We gathered a total of 10 scenes of C-band Radarsat-2 ultrafine mode single-look complex (SLC) images, covering the period from July 2021 to March 2022, with a revisit frequency of 24 days. Each image was obtained in VV polarization and a descending orbit. The SLC pixel spacing measured 1.33 m in the range direction and 2.01 m in the azimuth direction. Furthermore, we collected a total of 20 descending Sentinel-1A scenes in Interferometric Wide (IW) mode data (Orbit: Path 150 Frame 500) during the same time range, with the same polarization and orbit direction as the Radarsat-2 images. The Sentinel-1A data were downloaded from the Alaska Satellite Foundation Vertex website (https://vertex.daac.asf.alaska.edu/).

D. Auxiliary Data

We utilized a 12.5-m resolution upsampled digital elevation model (DEM) adopted in the ALOS PALSAR radiometrically
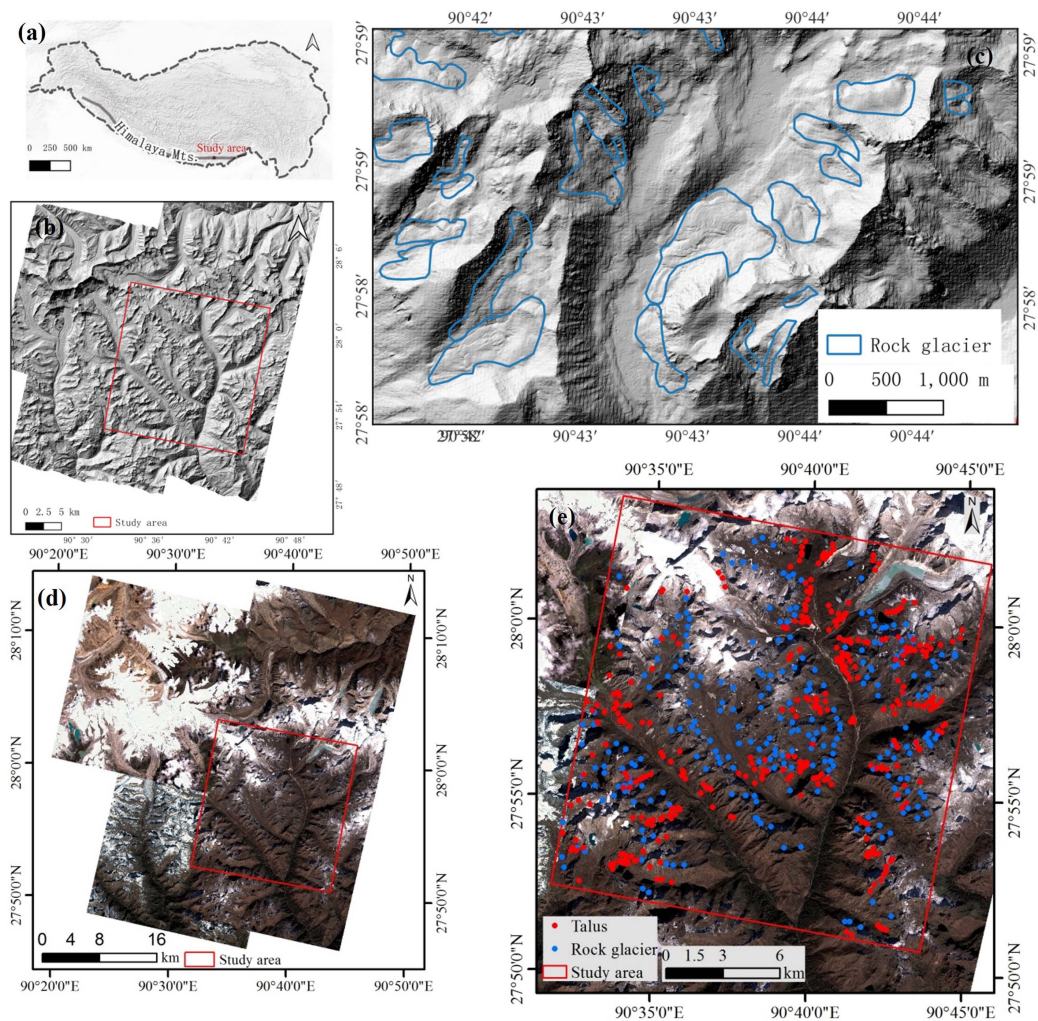
Fig. 1.   (a) Study area location. (b) Topography obtained from GF-7 stereo images and coverage of the Radarsat-2 SAR data. (c) Close-up view of the topography in a region with typical rock glaciers. (d) General view of GF-7 optical images. (e) Distribution of rock glaciers and talus in the study area.

TABLE I
INFORMATION ON THE GF-7 AND RADARSAT-2 IMAGES

Radatsat-2				GF-7		
No.	Acquisition date (dd/mm/yy)	No.	Acquisition date (dd/mm/yy)	No.	Acquisition date (dd/mm/yy)	Central Latitude and Longitude
1	09/07/21	6	30/11/21	1	13/12/21	E90.7_N28.1
2	02/08/21	7	24/12/21	2	11/08/22	E90.4_N27.9
3	19/09/21	8	17/01/22	3	07/12/21	E90.5_N27.9
4	13/10/21	9	10/02/22	4	13/12/21	E90.6_N27.9
5	06/11/21	10	06/03/22	5	11/08/22	E90.4_N28.1

terrain corrected (RTC), which was generated from a variety of DEM datasets, including the Shuttle Radar Topography Mission (SRTM) and NED. This DEM was employed to assess the accuracy of the DSM derived from GF-7 panchromatic stereoscopic images. The data were obtained from the Alaska Satellite Facility (ASF) Distributed Active Archive Center (DAAC) and can be found at https://asf.alaska.edu/data-sets/derived-data-sets/alos-palsar-rtc/alos-palsar-radiometric-terrain-correction/.

III. METHODS

This article presents a multibaseline PS and DS network-based MT-InSAR method for detecting rock glaciers and periglacial talus using multitemporal Radarsat-2 and Sentinel-1A SAR images. We conducted a detailed analysis of the activity characteristics of rock glaciers and periglacial talus at a fine scale. The overall processing chain is illustrated in Fig. 2.
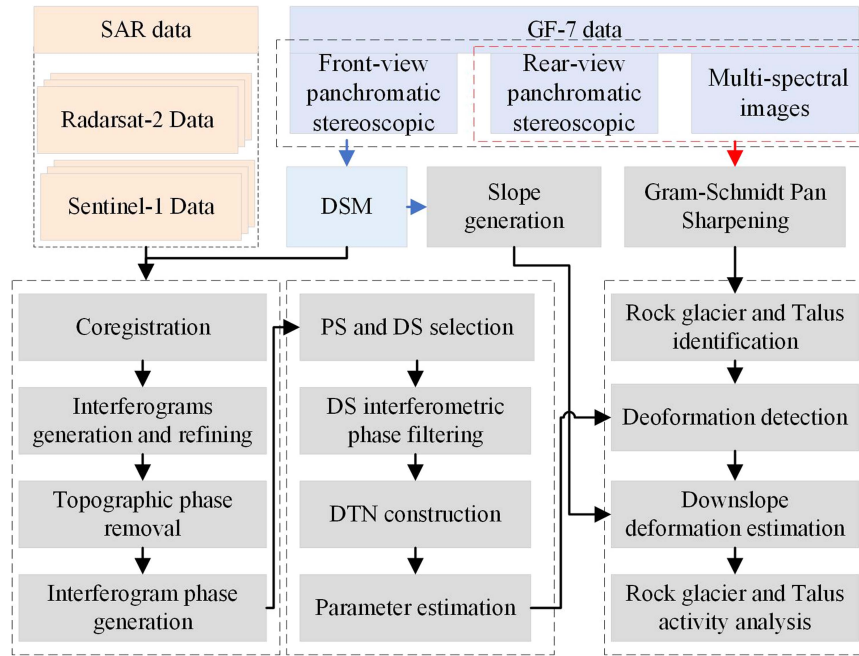
Fig. 2.   Flowchart of the proposed method.

A. Extraction of DSMs Using GF-7 Stereo Images

The process of extracting a DSM from optical stereo imagery involves a series of intricate steps. Fortunately, extensive research has been conducted in this field [40], [41], [42], [43]. To enhance the accuracy of optical remote sensing stereo mapping, we harnessed elevation control points derived from satellite laser altimetry (SLA) data [44], [45]. In this study, we leveraged GF-7 satellite SLA data and high-resolution stereo imagery to extract the DSM. The primary steps in extracting the high-precision DSM from stereo imagery are as follows. Initially, elevation control points are extracted from the SLA data obtained via the GF-7 satellite [46], [47]. Given that the study area is situated in a mountainous region, we relaxed the constraints for extracting elevation control points to increase their quantity. Subsequently, tie points are extracted from the high-resolution stereo imagery of the GF-7 satellite, and the laser elevation control points are matched with the stereo imagery [45]. Following this, a bundle adjustment is executed on the stereo imagery with the aid of laser elevation control points, elevating the overall accuracy of the study area [45]. Finally, a dense matching algorithm known as semiglobal matching is employed to extract the DSM of the study area [48]. With a maximum spatial resolution of 2 m, DSM products can be generated through dense matching of front and back images [49]. According to the application requirements of this study, the produced DSM products have a resolution of 4 m.

B. Identifying Rock Glacier and Talus Using GF-7 Optical Images

The identification and delineation of rock glaciers followed the established guidelines of the IPA action group on "Rock glacier inventories and kinematics" [24], [30]. This was carried out using cloud-free GF-7 multispectral and pan-color merged images. Leveraging the high resolution of GF-7 imagery (1 m), we identified 245 rock glaciers covering an approximate area of 400 km^2, with the smallest identified unit being 0.009 km^2.

Talus, a landform marked by the accumulation of loose, angular rock fragments, typically develops at the base of cliffs [2]. These talus slopes are prevalent in high mountain periglacial environments, such as the Rocky Mountains, Alps, Andes, Southern Alps, Sierra Nevada, and Hindu Kush Range [50]. The formation of talus primarily occurs over prolonged periods due to discrete rockfall events but is frequently altered by slope-face rockslide processes influenced by various individual or combined factors. In permafrost environments, these processes encompass avalanches, debris flows, frost action, permafrost creep, and the displacement of avalanche deposits [2]. Due to the diversity of debris slope forms, there are currently no standard guidelines for interpreting talus landforms. To address this, we referred to prior morphological studies on talus landforms [2], [51], [52], [53], [54]. This allowed us to identify a total of 351 periglacial talus by delineating their boundaries using GF-7 imagery [Fig. 1(e)].

C. Detecting Periglacial Landforms Deformation

The Radarsat-2 and Sentinel-1A SAR data underwent initial processing, which included coregistration and differential interferometry. Each interferogram was then multilooked, with factors of 8 and 2 for Sentinel-1A and 2 and 2 for Radarsat-2 in the range and azimuth directions, respectively. To ensure the accuracy of our analysis, we selected a small baseline network based on the average interferometric coherence of pixels within the area covering rock glaciers and talus [26], [28]. Interferograms with a mean coherence exceeding 0.6 were chosen for subsequent processing [26], [28].

To ensure an adequate number of monitoring points across the surfaces of rock glaciers and talus, initially, we selected the scatterers with a mean coherence exceeding 0.7 from all the chosen interferograms with small baselines, designating them as PS. To further enhance the density of measurement points, we then identified DS using a combination of statistically homogeneous pixels (SHPs) and the Anderson–Darling (AD) test. These DS points were subsequently adaptively filtered by leveraging SHP information and coherence weighting. The phase filter with SHP-based coherence weight was utilized to mitigate errors arising from low-coherence SHPs in the interferometric phase. The coherence-weight filtered interferometric phase (φ_{DS}) is defined as follows:

$$\varphi_{DS} = \frac{\sum_{i=1}^{N} coh_i \cdot \varphi_i}{N} \tag{1}$$

where φ_i represents the interferometric phase of SHPs, N is the count of SHPs, and coh_i is the mean coherence between the central pixel and the SHP in the time-series SAR images.

Subsequently, we constructed a Delaunay triangulation network (DTN) using the selected PS and DS points. This network facilitated the inversion of line of sight (LOS) deformation for rock glaciers and talus. The DTN plays a crucial role in removing the atmospheric phase screen (APS) through phase differencing of two adjacent pixels, assuming that the APS of adjacent pixels is similar. This step helps in mitigating atmospheric effects from the wrapped interferometric phase.

In the DTN network, the deformation gradients of interconnected arcs were resolved through the differential wrapped phase of connecting nodes. This was achieved using optimization techniques such as the Nelder-Mead, modified residue-signal ratio (RSR), and M-estimator algorithms [26]. To begin, long arcs with a spatial distance exceeding 400 m were excluded to eliminate arcs with significant differences in APS. The relative deformation rate between nodes within the arcs of the DTN was then determined by maximizing the absolute value of the temporal coherence (γ), as described as follows [55]:

$$\gamma = \frac{1}{N} \sum_{k=1}^{N} x_k \cdot \exp\left[j\left(\Delta\varphi_{phase}^k - \Delta\varphi_{model}^k\right)\right] / \sum_{k=1}^{N} x_k \tag{2}$$

in which N is the number of interferograms, x_k is the sum of the coherence connection nodes of the interferogram k, $\Delta\varphi_{phase}^k$ and $\Delta\varphi_{model}^k$ are the kth-measured and kth-modeled interferometric phase differences between the connection nodes.

The initial estimation of the relative deformation rate in the model interferometric phase was carried out using the local search Nelder–Mead algorithm, as described in previous works by Zhang et al. [26]. To enhance the robustness of the estimation, we introduced a modified Residue-Signal Ratio (RSR) to assess the effectiveness of the estimation of relative deformation parameters. RSR values exceeding a threshold of 0.3 indicated either an ineffectively calibrated APS or an inaccurate estimation of relative deformation parameters. In cases where RSR values exceeded this threshold, we employed an M-estimator to calculate the final deformation parameters [J in (5)]. This involved assigning smaller weights to larger phase residuals, improving

the accuracy of the estimation.

$$J^{(l)} = \left(D^T W^{(l)} D\right)^{-1} D^T W^{(l)} \Delta\varphi \tag{3}$$

$$D = \begin{bmatrix} 2\pi\xi_1 & 2\pi\eta_1 \\ \vdots & \vdots \\ 2\pi\xi_N & 2\pi\eta_N \end{bmatrix} \tag{4}$$

$$J = [h, v]^T. \tag{5}$$

In (3)–(5), $\Delta\varphi$ represents the temporal unwrapped phase, which was obtained based on preliminary estimates derived from (2) and the measured phase. Additionally, ξ is defined as $\xi = 2 b\_\perp/\lambda R$, and η as $\eta = 2 \Delta t/\lambda$, with Δt representing the period of the interferogram, b, λ, and R are the perpendicular baseline, wavelength, and slant range, respectively. l being the iteration index, parameter b, and W being an iteratively calculated weight matrix based on the phase residuals [26], [56].

Once the relative parameters for each arc were resolved, the absolute deformation parameters for each monitoring point were integrated using network adjustment. The integration was performed for the largest connected network using a ridge-estimator-based weighted least square approach.

$$S = \left(G^T W G + \sigma I\right)^{-1} G^T W H. \tag{6}$$

In the equation, S contains the absolute deformation parameters of the identified monitoring points. G is the adjustment matrix, composed of elements -1, 0, and 1. W represents the weight matrix, which takes into account the temporal coherence. H contains the estimated relative deformation parameters for the arcs, I is the identity matrix. To address issues related to global errors and ill-conditioned problems, a ridge estimator was introduced. In this study, the optimal parameter σ was determined through an iterative optimal estimation of the corner in dispersed L-curve sampling points. This was accomplished using the Menger curvature of a circumcircle and the golden section search method [26].

IV. RESULTS

A. Accuracy Evaluation of DSMs Extracted Using GF-7 Stereo Images

The overall result of DSM generated by GF-7 stereo images is shown in Fig. 1(b). The resolution of the DSM product is 4 m. We collected a total of 1050 GLAS points to assess the accuracy of the DSM product. The results indicate a high correlation between the GF-7 DSM product and GLAS elevation, with a correlation coefficient (R) of 0.96 and a root mean square error of 5.7 meters [Fig. 3(a)]. The elevation difference distribution histogram between GF-7 DSM and GLAS follows a Gaussian error distribution, with differences primarily concentrated within 10 m [Fig. 3(b)]. This concentration suggests the high accuracy of the DSM product extracted from GF-7 stereo images. It is worth noting that this study primarily utilized slope information generated from DSM products to analyze the relationship between the activity of periglacial landforms and terrain. Since the generation of DSM slope is mainly based on
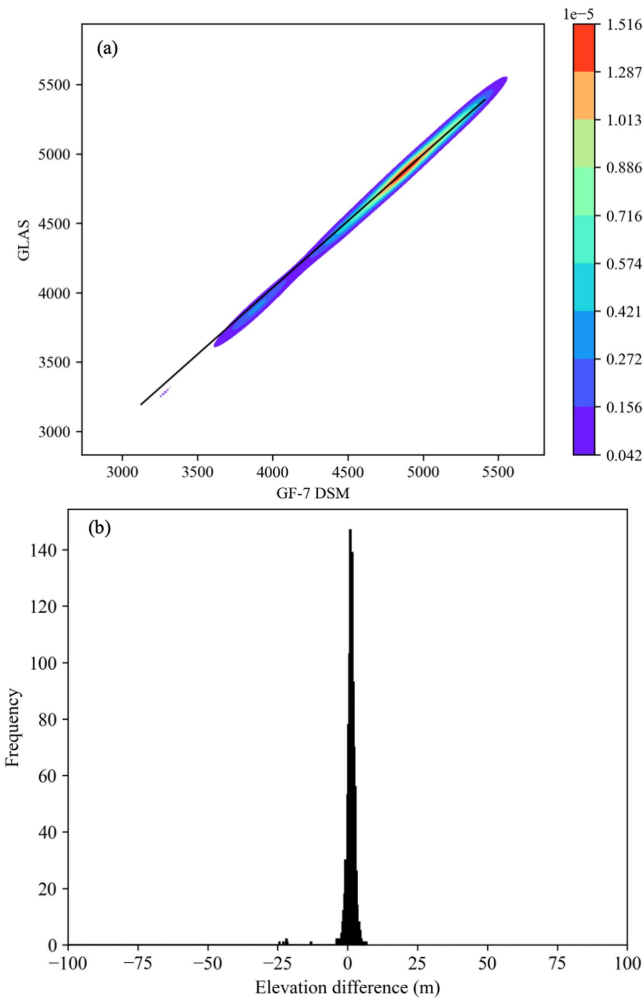
Fig. 3. (a) Density scatter between DSM generated by GF-7 and GLAS elevation. (b) Histogram of differential frequency distribution between GF-7 DSM and GLAS.

relative elevation, the influence of DSM errors on slope results is minimal. Therefore, the DSM products obtained in this study can provide high-precision, high-resolution slope information for periglacial landforms research.

B. LOS Deformation

The LOS deformation velocities of the total recognized periglacial landforms in the study area were obtained from Radarsat-2 and Sentinel-1A data with the proposed MT-InSAR method [Fig. 4(a)]. For a visual representation of the spatial deformation characteristics of these landforms, we employed a high-resolution DSM derived from GF-7 stereo imagery. This allowed us to create a high-resolution three-dimensional visualization alongside the deformation results. For example, in the case of rock glaciers, as shown in Fig. 5, Radarsat-2 provides more detailed insights into their activity. The spatial deformation within the rock glacier boundaries is better captured. While the overall trends in rock glacier activity between Radarsat-2 and Sentinel-1A are similar [see S3 region in Fig. 5(c) and (d)], some differences exist between the two datasets. In specific

TABLE II
ROCK GLACIER ACTIVITIES CLASSIFICATION RESULTS

Activity degree	Slope velocity	Radarsat-2 Counts	Sentinel-1 Counts
Relict	<1 cm/y	0	13
Transitional	1−3 cm/y	1	21
Transitional	3−10 cm/y	128	197
Active	10−30 cm/y	111	14
Active	>30 cm/y	5	0

areas, such as S1 and S2 in Fig. 5(c), Radarsat-2 results exhibit more comprehensive deformation details compared to Sentinel-1 [Fig. 5(c) and (d)]. Radarsat-2 data effectively detected deformation anomalies in some rock glaciers that were not evident in the Sentinel-1 results [see S4 region in Fig. 5(c) and (d)]. Furthermore, a comparison between Radarsat-2 deformation estimates and stereo-optical imagery reveals that rock glacier deformation mainly occurs in steeper slope areas, illustrating the topography impact on glacier movement [see S1-S4 regions in Fig. 5(b) and (c)]. These details are challenging to capture through two-dimensional optical imagery [Fig. 5(a)]. Thus, this study demonstrates that integrating high-resolution DSM, optical imagery, and deformation monitoring significantly enhances our understanding of periglacial landforms.

C. Rock Glacier Activities

The deformation rates obtained through the MT-InSAR method were measured in the SAR LOS direction. However, it is worth noting that most of the rock glaciers primarily move in the downslope direction [31]. To account for this, we initially projected the LOS velocities along the steepest slope direction [26], [28]. We conducted a statistical analysis, considering the 50th, 75th, and 100th percentiles of the downslope-parallel deformation velocities from all monitored pixels within each rock glacier's outline. The distribution of slope-parallel deformation for the rock glaciers across the study area is depicted in Fig. 6. The median value of the maximum deformation for rock glaciers in the study area reached 238.89 mm/y. By selecting the 75th percentile as a representation of the rock glaciers' activity, the median value of deformation within the study area was found to be 96.91 mm/y, indicating active rock glaciers in the study area.

To categorize the deformation velocity of the rock glaciers, we used the 75th percentile of the downslope-parallel deformation velocities from all monitored pixels within the rock glaciers' outlines, as recommended by Brencher et al. [32] and Zhang et al. [28]. We determined the activity type of each rock glacier by applying the slope-parallel deformation thresholds recommended by the IPA action group to the detected final deformation velocity [57]. On a regional scale, 47.5% (116 rock glaciers) were classified as active rock glaciers with slope deformation exceeding 100 mm/y (Table II). Another 128 rock glaciers were classified as transitional (Table II). We found that obvious deformation was observed in some of these transitional rock glaciers. When compared with the Sentinel-1A classification
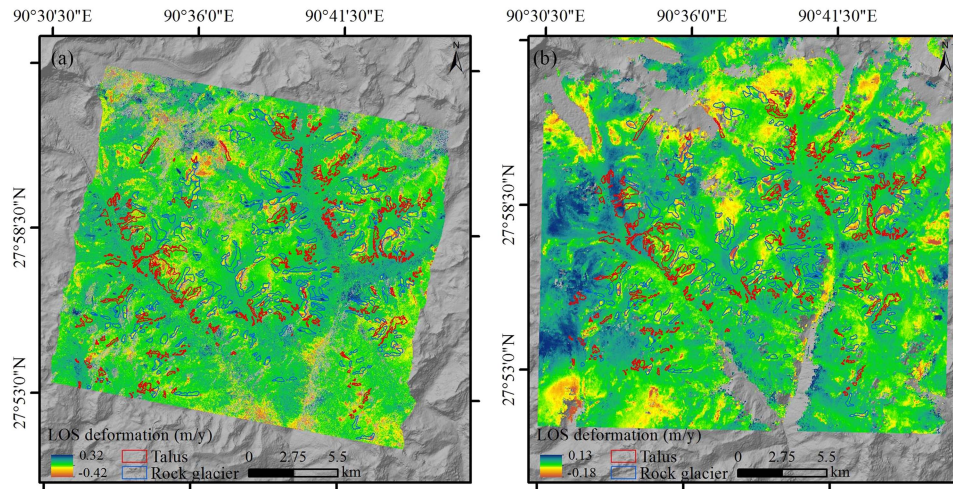
Fig. 4. LOS deformation velocities estimated by (a) Radarsat-2 and (b) Sentinel-1A data.
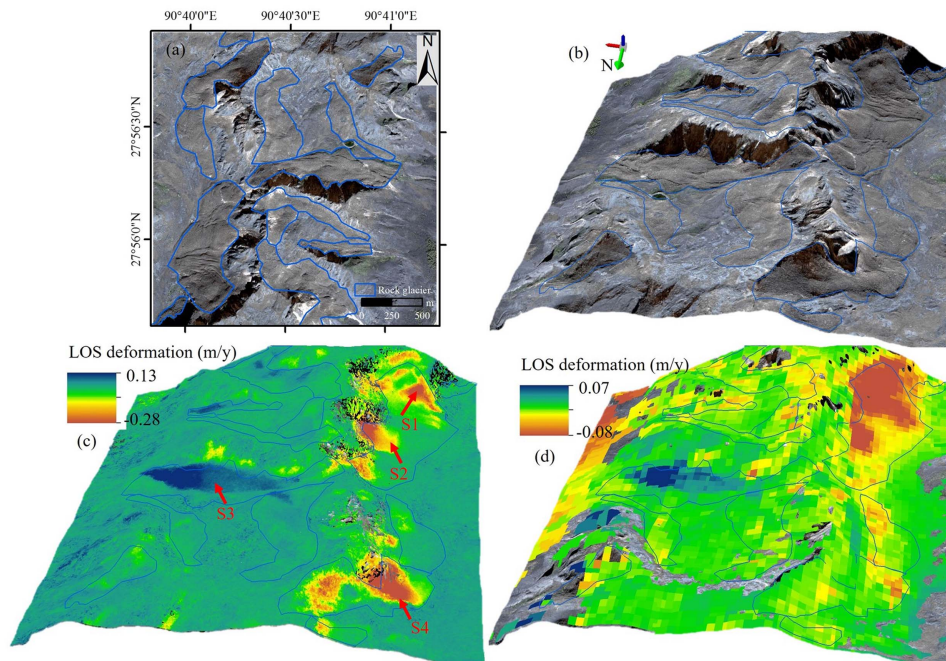

Fig. 5. (a) Optical imagery displaying the features of typical rock glaciers. (b) Three-dimensional representation of the rock glacier terrain, generated from GF-7 optical imagery and DSM. (c) LOS deformation monitoring results of the rock glacier using Radarsat-2 data. (d) LOS deformation monitoring results of the rock glacier using Sentinel-1A data.

results, Radarsat-2 identified a greater number of active rock glaciers (Table II).

In terms of morphology, rock glaciers can be categorized as tongue-shaped and lobate-shaped. Both morphologies include front, lateral margins, and optional ridge-and-furrow surface topography [30]. The geomorphological unit directly upslope of a rock glacier unit or system can provide insights into the characterization of the latter [30]. Regarding the spatial connection of rock glaciers to the upslope unit, as discerned from GF-7 optical images, two widely distributed types are glacier-connected and talus-connected within the study areas. To gain a deeper understanding of the deformation characteristics of rock

glaciers with different morphological structures, we selected the deformation velocity data of typical rock glaciers obtained from Radarsat-2 [Figs. 7(b), (e) and 8(b), (e)] and Sentinel-1A [Figs. 7(c), (f) and 8(c), (f)] using the proposed MT-InSAR method for analysis. The deformation monitoring results from Radarsat-2 and Sentinel-1 exhibit similar spatial distribution trends, confirming the effectiveness of the MT-InSAR method employed in this study. We analyzed typical glacier-connected tongue-shaped rock glaciers [Fig. 7(a)] and lobate-shaped rock glaciers [Fig. 7(d)] and talus-connected tongue-shaped rock glaciers [Fig. 8(a)] and lobate-shaped rock glaciers [Fig. 8(d)] across the study area. As shown in Fig. 7(a), a glacier-connected
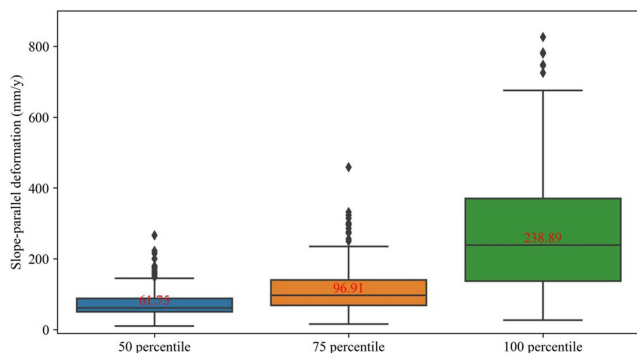
Fig. 6. Boxplot illustrating slope-parallel deformation of rock glaciers across the study area. The *x*-axis represents the statistical standards for each individual rock glacier, including the 50th percentile, 75th percentile, and 100th percentile.

tongue-shaped rock glacier displayed a pronounced ridge-and-furrow surface topography, corresponding to evident movement [Fig. 7(b) and (c)]. The deformation velocity of the front margins was reduced due to decreased material transport capacity and increased material accumulation compared to the ridge-and-furrow topography region. Additionally, as depicted in Fig. 7(a)–(c), the rock glacier is connected to a steep slope topography. Deformation anomalies on this steep slope were clearly visible in Radarsat-2 data but went undetected in Sentinel-1 data, emphasizing the advantages of using high-resolution Radarsat-2 for deformation monitoring.

Similar to tongue-shaped rock glaciers, glacier-connected lobate-shaped rock glaciers exhibited front, lateral margins, optional ridge-and-furrow surface topography, and a large developmental area [Fig. 7(d)]. The deformation velocity and topography within the rock glacier outline showed spatial heterogeneities, which were also observed in lobate-shaped rock glaciers, with relatively lower deformation velocities in this region [Fig. 7(e) and (f)].

Compared to glacier-connected rock glaciers, talus-connected rock glaciers exhibited a lower viscosity in terms of morphology, indicating a lower proportion of ice debris in talus-connected rock glaciers [Fig. 8(a) and (d)]. While a high deformation velocity was exhibited in talus-connected rock glaciers with tongue-shaped [Fig. 8(b) and (c)] and lobate-shaped [Fig. 8(e) and (f)] morphologies. Therefore, in certain scenarios, the ice content within the debris may not be the primary factor influencing the activity of talus-connected rock glaciers. Factors such as the geomorphic environment in which the ice glacier develops, the ice content within the ice core layer, and external climatic conditions could potentially be critical factors affecting the movement of talus-connected rock glaciers.

The ridge-and-furrow surface topography was an optional feature for discriminating the rock glaciers. As shown in Fig. 8(a), the surface of a talus-connected tongue-shaped rock glacier appeared uniform without a ridge-and-furrow structure, yet it exhibited clear activity. This suggests that relying solely on morphology from optical images may not accurately determine the activity of rock glaciers. MT-InSAR is a crucial technique for investigating the activity dynamics of rock glaciers. Fig. 8(b)

depicts a typical talus-connected lobate-shaped rock glacier, where the talus delivered debris to the rock glacier. The upslope of the rock glacier has a steep slope and serves as a material source, correspondingly, obvious deformation is occurring in this region. As the slope gradually becomes gentler and debris accumulates, the rock glacier progressively develops ridge-and-furrow topography, likely attributed to insufficient gravity force and a lower ice content within the ice core layer, resulting in less pronounced deformation at the rock glacier's front edge and ridge-and-furrow topography region [Fig. 8(e) and (f)].

Through the analysis of the morphologies and deformation velocities of different typical rock glacier types, it becomes evident that rock glacier activity cannot be easily determined based solely on morphology. Deformation velocities of different surface structures within rock glacier morphological outlines exhibit significant spatial heterogeneity. Typically, deformation rates are lower at the front margins, and the activity of ridge-and-furrow topography varies significantly among different rock glaciers.

D. Talus Activities

Differing from rock glaciers with distinct and unique morphological characteristics, talus displays notable diversity in terms of profiles, size, and other attributes. The identification of talus morphology was made possible through high-resolution GF-7 optical imagery. Similar to the statistical analysis for rock glaciers in Fig. 6, we conducted a statistical analysis of the 50th, 75th, and 100th percentiles of the downslope-parallel deformation velocities for all monitored pixels within the individual talus outlines.

For all the talus in the study area, the median deformation rate was 37.85 mm/y in the 50th percentile, 44.69 mm/y in the 75th percentile, and 51.24 mm/y in the 100th percentile (Fig. 9). When compared to the rock glacier landforms (Fig. 6), talus generally exhibited lower deformation velocities (Fig. 9). Some small-scale talus are typically in a stable state, while larger talus exhibit significant spatial heterogeneity, with deformation zones typically concentrated in a smaller portion (Fig. 10). The lower activity of talus compared to rock glaciers can be attributed to two factors. First, talus typically contains less internal ice, experiencing less influence from freeze-thaw processes and temperature variations. Their primary driving forces are gravity and the thickness of surface debris. Second, unlike the continuous movement of rock glaciers, the sliding of talus can occur rapidly and come to an end swiftly, which may not be captured by InSAR techniques.

Although high-resolution optical imagery has provided an effective foundation for identifying talus, in some cases, orthoimagery can obscure slope information. Due to the less distinct morphological characteristics of talus compared to rock glaciers, this can lead to issues of misidentification of talus.

As shown in Fig. 11, some talus [e.g., the talus within the white rectangle in Fig. 11(a)] were hard to recognize but were discovered after being displayed in three dimensions [Fig. 11(b)]. Furthermore, the deformation in these areas was also significant in the deformation monitoring results [Fig. 11(c)]. Therefore, in
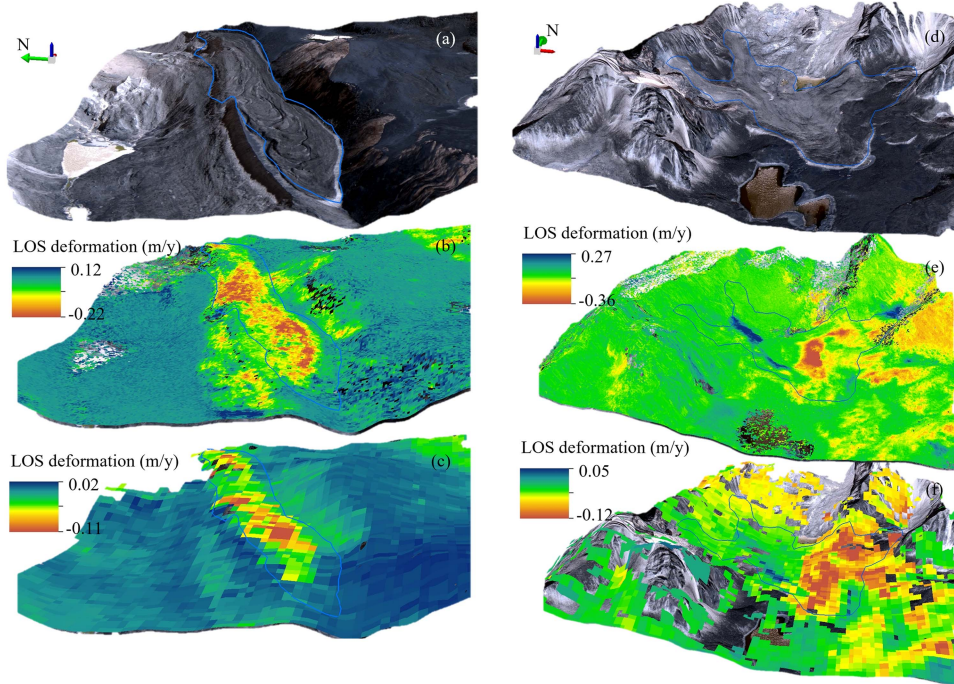
Fig. 7. Three-dimensional GF-7 optical imagery of typical glacier-connected tongue-shaped (location:28°1′30″N, 90°41′0″E) (a) and lobate-shaped (location:28°0′18″N, 90°35′39″E) (d) rock glaciers. Additionally, (b) and (e) display the LOS deformation monitoring results of typical glacier-connected tongue-shaped (a) and lobate-shaped (d) rock glaciers using Radarsat-2 data, while (c) and (f) showcase the LOS deformation monitoring results of typical glacier-connected tongue-shaped (a) and lobate-shaped (d) rock glaciers using Sentinel-1A data.
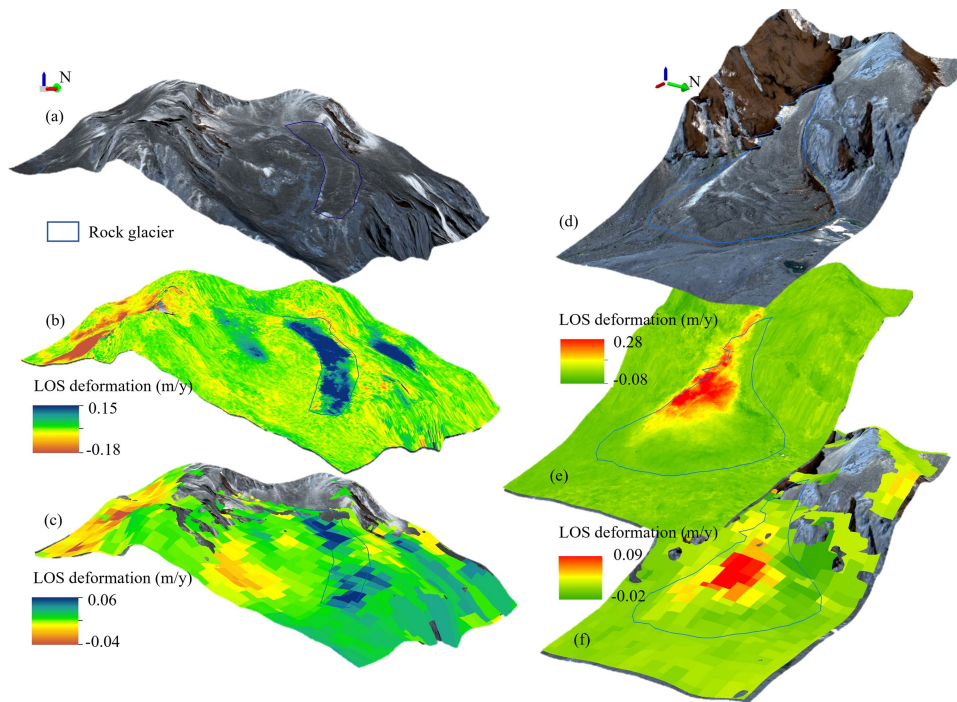

Fig. 8. Three-dimensional GF-7 optical imagery of typical talus-connected tongue-shaped (location:28°0′24″N, 90°39′30″E) (a) and lobate-shaped (location:27°55′53″N, 90°37′0″E) (d) rock glaciers. Additionally, (b) and (e) display the LOS deformation monitoring results of typical talus-connected tongue-shaped (a) and lobate-shaped (d) rock glaciers using Radarsat-2 data, while (c) and (f) showcase the LOS deformation monitoring results of typical talus-connected tongue-shaped (a) and lobate-shaped (d) rock glaciers using Sentinel-1A data.
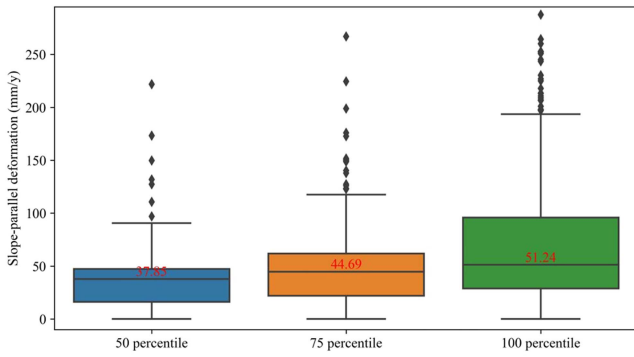
Fig. 9. Boxplot illustrating slope-parallel deformation of talus across the study area. The *x*-axis represents the statistical standards for each individual talus, including the 50th percentile, 75th percentile, and 100th percentile.
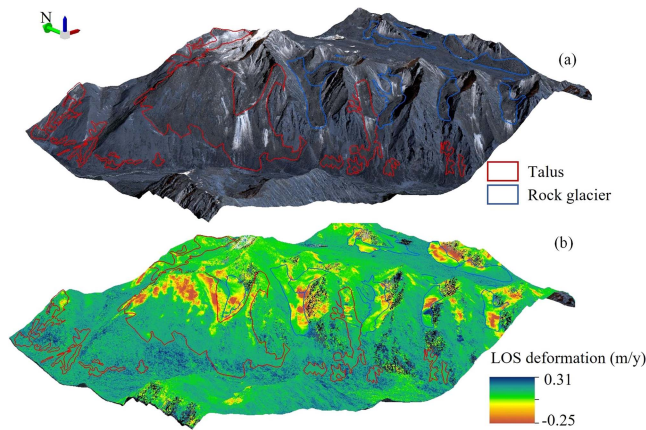

Fig. 10. (a) Three-dimensional GF-7 optical imagery of typical talus(location:28°0′33″N, 90°40′36″E). (b) LOS deformation monitoring results of typical talus acquired by Radarsat-2 data.

addition to high-resolution optical imagery recognition, the integration of high-resolution topographic data and high-resolution MT-InSAR deformation monitoring information can effectively enhance the identification of talus.

V. DISCUSSION

A. Accuracy of MT-InSAR Results

Previously, we used the multibaseline PS and DS combined MT-InSAR method to monitor rock glacier activity in the central Himalayas using Sentinel-1 data. We conducted a cross-comparison between the proposed MT-InSAR method and the SBAS method, preliminarily validating the effectiveness of our approach [26]. In the process of surface deformation estimation, atmospheric phase delay is a crucial factor affecting the accuracy of deformation observation results. Network differencing of monitoring points and improvements in the RSR assessment criteria can effectively eliminate the influence of topography-related atmospheric phase. In terms of the computational efficiency of the proposed MT-InSAR method, the deformation parameter solving process of the multibaseline PS-DS combined network method is lower than that of the SBAS method. However, the SBAS method requires phase unwrapping
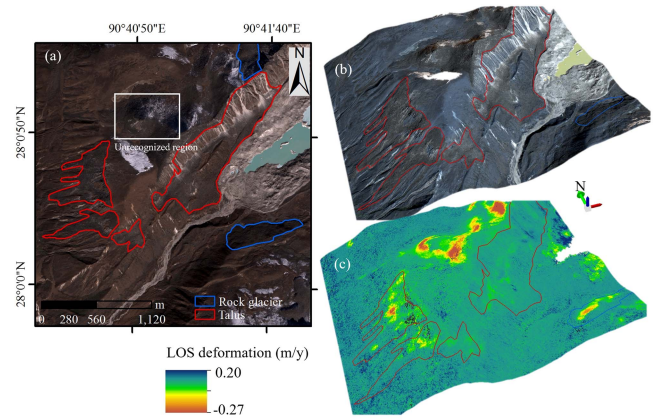

Fig. 11. (a) Optical imagery characteristics of the typical talus. (b) Three-dimensional representation of the study terrain, which is generated by GF-7 optical imagery and DSM. (c) LOS deformation monitoring results of the rock glaciers and talus using Radarsat-2 data.

operations, which increases the overall time required to obtain the final deformation results. The method applied in this study involves a network integration process, utilizing a weighted least squares-ridge estimation algorithm. The implementation of ridge estimation relies on determining the optimal regularization parameter, achieved through the use of the L-Curve to determine the optimal regularization parameter dependent on the truncated singular value decomposition (TSVD) method for solving equations. The computation efficiency of deformation solving is unavoidably reduced by the determination of the eigenvalues and eigenvectors of the super-large matrix TSVD. The introduced Menger curvature of a circumcircle and the golden section search method in this paper can greatly improve the computational efficiency of point operations based on the network differencing method.

In this study, we applied the method to Radarsat-2 data (Fig. 12), we can observe that the extracted results from Radarsat-2 data are in good spatial consistency with those obtained from Sentinel-1 data, with a correlation of 0.65 [Fig. 12(c)]. Notably, the high resolution of Radarsat-2 enables it to differentiate active displacements occurring on smaller-scale rock glacier landforms [Fig. 12(b)]. Furthermore, the monitoring values of active rock glaciers using Radarsat-2 high-resolution SAR data are generally higher than those of Sentinel-1 results [Fig. 12(c)]. Sentinel-1A data tends to underestimate the true activity of the rock glacier compared to Radarsat-2 data. This underestimation can be attributed to the spatial averaging of Sentinel-1 data, which may miss smaller rock glacier features with strong displacement trends. Additionally, due to the relatively low spatial resolution of Sentinel-1 data compared with Radarsat-2, the spatial extent of the deformation signal may not adequately capture fast deformation fringes. Some studies have indicated differences in the observational levels between Radarsat-2 and Sentinel-1 data, with Radarsat-2 being capable of capturing subsidence down to −10 centimeters, whereas Sentinel-1 captured subsidence down to −4.5 cm or −2.5 cm using different multilooking modes [58]. Moreover, the different incidence angles of Sentinel-1 and Radarsat-2 data contribute to
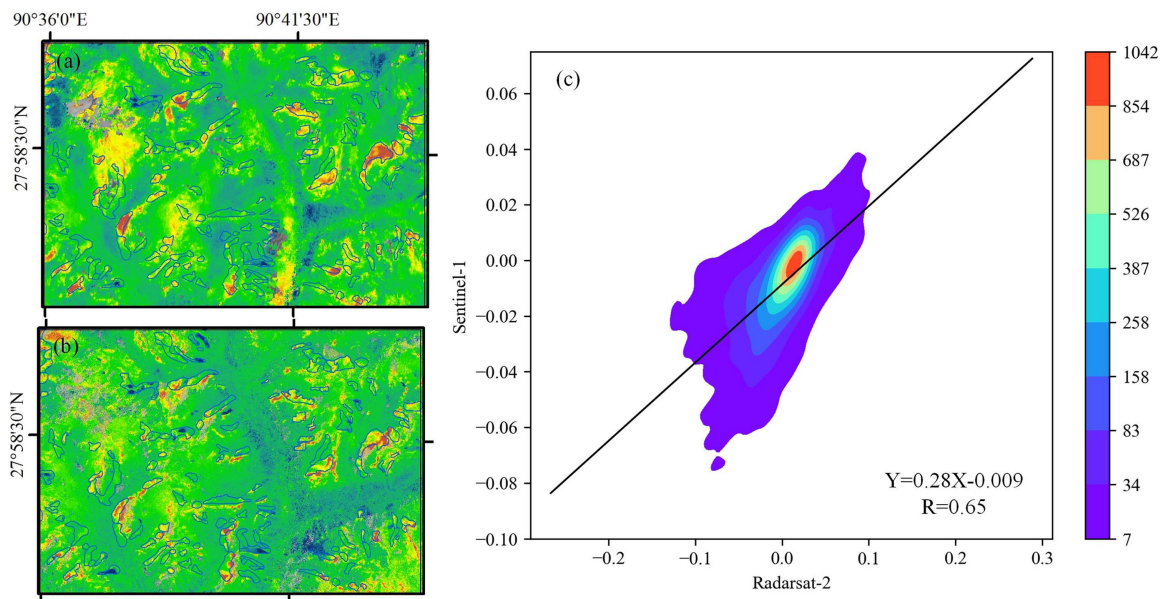
Fig. 12.   LOS deformation velocities estimated by (a) Sentinel-1A and (b) Radarsat-2 data. (c) Density scatter plot comparing Radarsat-2 and Sentinel-1A data results.

variations in the observed LOS deformation values [59], [60]. It is important to note that the limited capability of InSAR to detect movement perpendicular to the LOS direction presented challenges in accurately determining the deformation status of certain rock glaciers and talus formations facing north or south.

Periglacial landforms, especially surface geometry changes in rock glaciers, have been quantified at fine scales using methods such as UVA surveys, and terrestrial and airborne laser scanning [61]. These approaches provide effective means for investigating periglacial landform movement, but their use is limited by high costs and challenging environmental conditions. As a result, the focus of high-resolution deformation detection has been primarily on single-rock glaciers. In this study, we quantitatively captured the deformation characteristics of typical rock glaciers and talus at a regional scale with high resolution [Figs. 11(b) and 12(b)]. It is clear that Radarsat-2 high-resolution data outperforms Sentinel-1 IW mode data in capturing finer details of terrain deformation. Despite Radarsat-2's 24-day revisit cycle, the ultrafine mode data maintains strong coherence retention capabilities in rock glacier and talus terrain, demonstrating the suitability of high-resolution Radarsat-2 SAR data for quantifying the spatial and temporal dynamics of periglacial landforms in complex topographical environments.

In recent years, space agencies worldwide have shown increasing interest in the development of high-resolution SAR systems operating at the L-band due to its superior penetration capabilities compared to the X and C-bands. This is evident from the successful L-band systems already in operation, such as SAOCOM-1A/B [62] and Lu Tan-1A/B [63]. For example, Lu Tan-1 (LT-1) is the first L-band SAR satellite constellation with a repeat orbit of 8 days for a single satellite and 4 days for two satellites, and it offers a resolution of 3 m in stripmap1 mode. It is foreseeable that with the continued development of high-resolution SAR satellites, the monitoring of periglacial

landform deformation based on high-resolution SAR data and InSAR technology will have broad applications at regional scales with high resolution.

B. Deformation Characteristics of Rock Glaciers

Gravity-driven creep of debris and interstitial ice are key indicators of an active rock glacier [64]. Previous studies have suggested that environmental factors play a crucial role in controlling the variability of rock glacier flow on interannual and annual time scales [28]. The correlations between precipitation, freeze-thaw events, altitude, permafrost occurrence probability, and activity were found in our previous study [28]. To comprehensively analyze the impact of gravitational forces on the movement of rock glaciers, we extracted deformation and topographic profiles from representative rock glaciers to quantitatively assess the relationship between deformation and topography (Fig. 13).

From the profiles of these representative rock glaciers [P1-P2, P3-P4, P5-P6 in Fig. 13(a)], it can be observed that in areas with gentler slopes (<20°), the corresponding deformation is lower [Fig. 13(c) and (d)]. Conversely, in regions with steeper slopes or significant slope variations [Fig. 13(b)–(d)], deformation noticeably increased or exhibited obvious oscillations. However, it is evident that in areas with extremely steep slopes, deformation values do not increase with slope steepness. Instead, they exhibit decreased activity [Fig. 13(d)]. This is likely because steep slopes can trigger rapid movement in rock glaciers but are not conducive to the long-term retention of debris material. This leads to predominantly stable conditions over most of the time, with movement beginning after debris material has sufficiently accumulated. As shown in Fig. 13(b), in certain areas with relatively minor slope variations, there are observed differences in deformation intensity and a continuous changing
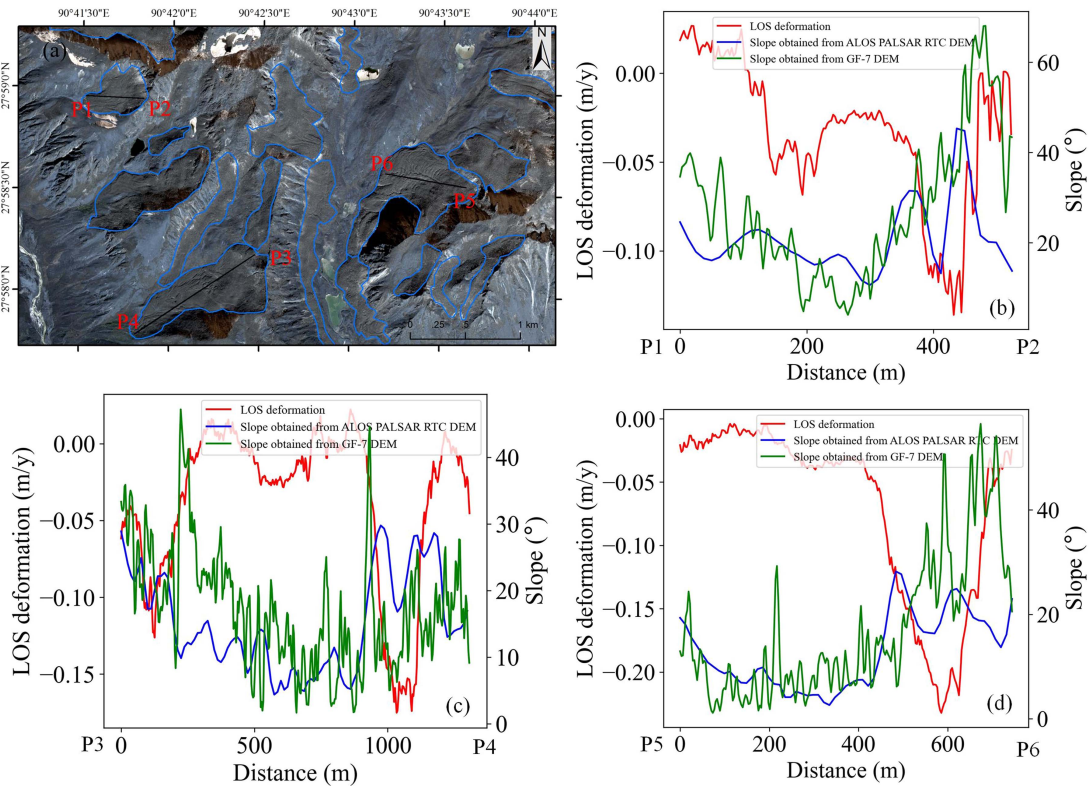
Fig. 13. (a) Optical imagery characteristics of the typical rock glaciers. (b), (c), and (d) are the LOS deformation and slope profile of P1-P2, P3-P4, and P5-P6 in (a), respectively.

trend within the rock glacier. This indicates that, apart from slope, the deformation of rock glaciers is also influenced by other factors, such as variations in ice content within the ice core layer of the rock glacier.

C. Deformation Characteristics of Talus

During the evolution of periglacial landforms, the ice content beneath the surface gravel gradually decreases from massive ice deposits to soil matrix ice lenses, and the talus is an integral part of the periglacial landform evolution, transitioning from debris glacier to rock glaciers and talus [4]. The difference in ice content between talus and rock glaciers can be visually distinguished from optical images (Figs. 7 and 10). Therefore, unlike the movement of rock glaciers, which is primarily influenced by internal ice content, and topography, the movement of rock slopes is mainly influenced by the slope of the terrain and the surface gravel coverage of the landform itself [65]. Clearly, the downslope paths of rockfall debris of talus are strongly influenced by overall talus relief and detailed surface roughness and hardness [2]. As shown in Fig. 14, there are significant spatial differences in the content of surface debris cover within the talus contour, with some areas exposed to bedrock. Correspondingly, the obvious deformation is mainly concentrated in areas with more surface debris cover [Fig. 14(b)]. In addition, the activity of talus in areas with debris cover shows a significant response relationship with slope gradient, indicating the influence of topography on the movement of talus [Fig. 14(b)].
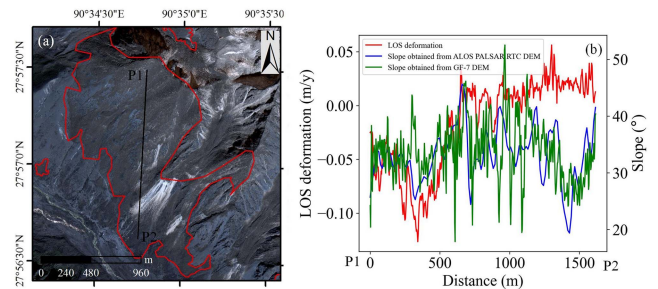

Fig. 14. (a) Optical imagery of the typical talus. (b) LOS deformation and slope profile of P1-P2 in (a).

VI. Conclusion

In this study, we employed the MT-InSAR method to monitor the deformation of periglacial landforms in the Eastern Himalayas. High-resolution GF-7 optical images and Radarsat-2 SAR data allowed us to identify 245 rock glaciers and 351 talus deformations. Our analysis focused on the fine-scale deformation characteristics of these rock glaciers and talus, leading to the following main conclusions:

The Radarsat-2 findings offer a nuanced and thorough perspective on spatial deformation within periglacial landforms, surpassing Sentinel-1 data. Specifically, analysis of Radarsat-2 data showed that 47.5% (116) of identified rock glaciers were classified as active. Conversely, talus deformations in the Eastern

Himalayas exhibited lower levels of activity compared to rock glaciers.

The morphology of glacier-connected tongue-shaped and lobate-shaped rock glaciers is defined by prominent ridge-and-furrow surface features, reflecting their unique movement patterns. The front margins of these rock glaciers demonstrate decreased deformation velocity attributed to reduced material transport and increased accumulation. However, spatial heterogeneity is notably evident, especially in lobate-shaped rock glaciers.

Environmental factors such as precipitation, freeze-thaw processes, and gravity-driven forces are pivotal in dictating rock glacier movement. While deformation in certain rock glaciers correlates strongly with slope topography, the intricate process of rock glacier development demands a holistic approach considering diverse factors, such as topographic terrain, climatic conditions, surface composition, internal structure, and ice content. Conversely, talus landforms display notable spatial variability in deformation, with pronounced deformation mainly clustered in regions with greater surface debris cover. Terrain slope and gravel coverage on the surface of the landform are the primary influencers of talus movement.

The application of multisource data can effectively enhance the depth of research into periglacial landforms geomorphology kinematics. In this study, high-resolution optical data were used to accurately identify the contours of glacial landforms and obtain high-resolution topographic information. Building upon this, high-resolution SAR data were employed to capture the spatial deformation characteristics of rock glaciers and talus slopes, demonstrating the value of high-resolution SAR data in periglacial research. It can be anticipated that with the utilization of long-term, high-frequency, high-resolution SAR data, we will be able to not only acquire the spatial characteristics of periglacial landforms but also capture their temporal dynamics and their responses to environmental changes. This will further enhance our understanding of the spatiotemporal kinematics of periglacial landforms.

REFERENCES

[1] J. R. Janke and T. Bolch, "4.06-rock glaciers," in *Treatise On Geomorphology*, 2nd ed., J. F. Shroder, Ed. New York, NY, USA: Academic, 2022, pp. 75–118.

[2] B. H. Luckman, "Permafrost and periglacial features|talus slopes," in *Encyclopedia of Quaternary Science*, 2nd ed., S. A. Elias and C. J. Mock, Ed. Amsterdam, The Netherlands: Elsevier, 2013, pp. 566–573.

[3] A. Kääb, "Rock glaciers," in *Reference Module in Earth Systems and Environmental Sciences*. Amsterdam, The Netherlands: Elsevier, 2022.

[4] W. B. Whalley and H. E. Martin, "Rock glaciers: II models and mechanisms," *Prog. Phys. Geography: Earth Environ.*, vol. 16, no. 2, pp. 127–186, 1992.

[5] A. Bartsch, T. Strozzi, and I. Nitze, "Permafrost monitoring from space," *Surv. Geophys.*, vol. 44, no. 5, pp. 1579–1613, 2023.

[6] P.-A. Duvillard, L. Ravanel, M. Marcer, and P. Schoeneich, "Recent evolution of damage to infrastructure on permafrost in the French Alps," *Regional Environ. Change*, vol. 19, no. 5, pp. 1281–1293, 2019.

[7] J. Hassan, X. Chen, S. Muhammad, and N. A. Bazai, "Rock glacier inventory, permafrost probability distribution modeling and associated hazards in the Hunza River Basin, Western Karakoram, Pakistan," *Sci. Total Environ.*, vol. 782, 2021, Art. no. 146833.

[8] H. Ø. Eriksen et al., "Recent acceleration of a rock glacier complex, Ádjet, Norway, documented by 62 years of remote sensing observations," *Geophysical Res. Lett.*, vol. 45, no. 16, pp. 8314–8323, 2018.

[9] A. Cicoira, J. Beutel, J. Faillettaz, I. Gärtner-Roer, and A. Vieli, "Resolving the influence of temperature forcing through heat conduction on rock glacier dynamics: A numerical modelling approach," *Cryosphere*, vol. 13, no. 3, pp. 927–942, 2019.

[10] S. Buchelt et al., "Deciphering small-scale seasonal surface dynamics of rock glaciers in the central European Alps using DInSAR time series," *Remote Sens.*, vol. 15, no. 12, 2023, Art. no. 2982.

[11] M. Cignetti et al., "Taking advantage of the ESA G-POD service to study ground deformation processes in high mountain areas: A valle d'aosta case study, Northern Italy," *Remote Sens.*, vol. 8, no. 10, 2016, Art. no. 852.

[12] L. Rouyet et al., "Evidence of rock slope breathing using ground-based InSAR," *Geomorphology*, vol. 289, pp. 152–169, 2017.

[13] V. Wirz et al., "Short-term velocity variations at three rock glaciers and their relationship with meteorological conditions," *Earth Surf. Dyn.*, vol. 4, no. 1, pp. 103–123, 2016.

[14] A. Bertone et al., "Unprecedented observation of hourly rock glacier velocity with ground-based SAR," *Geophysical Res. Lett.*, vol. 50, no. 9, 2023, Art. no. e2023GL102796.

[15] S. Vivero, H. Hendrickx, A. Frankl, R. Delaloye, and C. Lambiel, "Kinematics and geomorphological changes of a destabilising rock glacier captured from close-range sensing techniques (Tsarmine rock glacier, Western Swiss Alps)," *Front. Earth Sci.*, vol. 10, 2022, Art. no. 1017949.

[16] T. Groh and J. H. Blöthe, "Rock glacier kinematics in the Kaunertal, Ötztal Alps, Austria," *Geosciences*, vol. 9, no. 9, 2019, Art. no. 373.

[17] E. Bollmann, A. Girstmair, S. Mitterer, K. Krainer, R. Sailer, and J. Stötter, "A rock glacier activity index based on rock glacier thickness changes and displacement rates derived from airborne laser scanning," *Permafrost Periglacial Processes*, vol. 26, no. 4, pp. 347–359, 2015.

[18] J. H. Blöthe, C. Halla, E. Schwalbe, E. Bottegal, D. T. Liaudat, and L. Schrott, "Surface velocity fields of active rock glaciers and ice-debris complexes in the central Andes of Argentina," *Earth Surf. Processes Landforms*, vol. 46, no. 2, pp. 504–522, 2021.

[19] C. Lambiel, T. Strozzi, N. Paillex, S. Vivero, and N. Jones, "Inventory and kinematics of active and transitional rock glaciers in the Southern Alps of New Zealand from Sentinel-1 InSAR," *Arctic, Antarctic, Alpine Res.*, vol. 55, no. 1, 2023, Art. no. 2183999.

[20] C. Barboux, T. Strozzi, R. Delaloye, U. Wegmüller, and C. Collet, "Mapping slope movements in Alpine environments using TerraSAR-X interferometric methods," *ISPRS J. Photogrammetry Remote Sens.*, vol. 109, pp. 178–192, 2015.

[21] C. Barboux, R. Delaloye, and C. Lambiel, "Inventorying slope movements in an Alpine environment using DInSAR," *Earth Surf. Processes Landforms*, vol. 39, no. 15, pp. 2087–2099, 2014.

[22] T. Strozzi et al., "Monitoring rock glacier kinematics with satellite synthetic aperture radar," *Remote Sens.*, vol. 12, no. 3, pp. 1–23, 2020.

[23] L. Liu, C. I. Millar, R. D. Westfall, and H. A. Zebker, "Surface motion of active rock glaciers in the Sierra Nevada, California, USA: Inventory and a case study using InSAR," *Cryosphere*, vol. 7, no. 4, pp. 1109–1119, 2013.

[24] A. Bertone et al., "Incorporating InSAR kinematics into rock glacier inventories: Insights from 11 regions worldwide," *Cryosphere*, vol. 16, no. 7, pp. 2769–2792, 2022.

[25] J. Cai, X. Wang, G. Liu, and B. Yu, "A comparative study of active rock glaciers mapped from geomorphic- and kinematic-based approaches in Daxue Shan, Southeast Tibetan Plateau," *Remote Sens.*, vol. 13, no. 23, 2021, Art. no. 4931.

[26] X. Zhang et al., "Detecting rock glacier displacement in the central Himalayas using multi-temporal InSAR," *Remote Sens.*, vol. 13, no. 23, 2021, Art. no. 4738.

[27] X. Wang, L. Liu, L. Zhao, T. Wu, Z. Li, and G. Liu, "Mapping and inventorying active rock glaciers in the northern Tien Shan of China using satellite SAR interferometry," *Cryosphere*, vol. 11, no. 2, pp. 997–1014, 2017.

[28] X. Zhang et al., "Kinematic inventory of rock glaciers in the Nyainqêntanglha Range using the MT-InSAR method," *Int. J. Digit. Earth*, vol. 16, no. 1, pp. 3923–3948, 2023.

[29] RGIK, "Towards standard guidelines for inventorying rock glaciers: Practical concepts (V2.0). IPA action group rock glacier inventories and kinematics," 2022. [Online]. Available: Current_Practical_Concepts_Inventorying_Rock_Glaciers.pdf(unifr.ch)

[30] RGIK, "Towards standard guidelines for inventorying rock glaciers: Baseline concepts (version 4.2.2). IPA action group rock glacier inventories and kinematics," 2022. [Online]. Available: https://bigweb.unifr.ch/Science/Geosciences/Geomorphology/Pub/Website/IPA/Guidelines/V4/220331_Baseline_Concepts_Inventorying_Rock_Glaciers_V4.2.2.pdf

[31] E. Reinosch, M. Gerke, B. Riedel, A. Schwalb, Q. Ye, and J. Buckel, "Rock glacier inventory of the western Nyainqêntanglha Range, Tibetan Plateau, supported by InSAR time series and automated classification," *Permafrost Periglacial Processes*, vol. 32, no. 4, pp. 657–672, 2021.

[32] G. Brencher, A. L. Handwerger, and J. S. Munroe, "InSAR-based characterization of rock glacier movement in the Uinta Mountains, Utah, USA," *Cryosphere*, vol. 15, no. 10, pp. 4823–4844, 2021.

[33] Y. Hu et al., "Mapping and characterizing rock glaciers in the arid western Kunlun mountains supported by InSAR and deep learning," *J. Geophysical Res.: Earth Surf.*, vol. 128, no. 9, 2023, Art. no. e2023JF007206.

[34] D. A. Bonneau and D. J. Hutchinson, "The use of terrestrial laser scanning for the characterization of a cliff-talus system in the Thompson River Valley, British Columbia, Canada," *Geomorphology*, vol. 327, pp. 598–609, 2019.

[35] F. L. Pérez, "Talus movement in the high equatorial Andes: A synthesis of ten years of data," *Permafrost Periglacial Processes*, vol. 4, no. 3, pp. 199–215, 1993.

[36] F. Imaizumi, T. Nishiguchi, N. Matsuoka, D. Trappmann, and M. Stoffel, "Interpretation of recent alpine landscape system evolution using geomorphic mapping and L-band InSAR analyses," *Geomorphology*, vol. 310, pp. 125–137, 2018.

[37] B. Dini, S. Daout, A. Manconi, and S. Loew, "Classification of slope processes based on multitemporal DInSAR analyses in the Himalaya of NW Bhutan," *Remote Sens. Environ.*, vol. 233, 2019, Art. no. 111408.

[38] A. Bhattacharya and K. Mukherjee, "Review on InSAR based displacement monitoring of Indian Himalayas: Issues, challenges and possible advanced alternatives," *Geocarto Int.*, vol. 32, no. 3, pp. 298–321, 2017.

[39] Y. Kang, Z. Lu, C. Zhao, Y. Xu, J.-W. Kim, and A. J. Gallegos, "InSAR monitoring of creeping landslides in mountainous regions: A case study in Eldorado National Forest, California," *Remote Sens. Environ.*, vol. 258, 2021, Art. no. 112400.

[40] P. Reinartz, P. Angelo, T. Krauß, and H. Chaabouni-Chouayakh, "DSM generation and filtering from high resolution optical stereo satellite data," in *Proc. 30th Eur. Assoc. Remote Sens. Lab. (EARSeL) Symp.*, Paris, France, May 31–Jun. 3, 2010, pp. 527–536.

[41] K. Gong and D. Fritsch, "A detailed study about digital surface model generation using high resolution satellite stereo imagery," *ISPRS Ann. Photogrammetry, Remote Sens., Spatial Inf. Sci.*, vol. III-1, pp. 69–76, 2016.

[42] M. Rothermel, K. Wenzel, D. Fritsch, and N. Haala, "SURE: Photogrammetric surface reconstruction from imagery," in *Proc. LC3D Works Workshop. Vis.*, 2012, Art. no. 2.

[43] Y. Zhou and M. Duan, "A batch postprocessing method based on an adaptive data partitioning strategy for DEM differencing from global data products," *IEEE Geosci. Remote Sens. Lett.*, vol. 21, 2024, Art. no. 2000705.

[44] G. Zhang, K. Xu, P. Jia, X. Hao, and D. Li, "Integrating stereo images and laser altimeter data of the ZY3-02 satellite for improved earth topographic modeling," *Remote Sens.*, vol. 11, no. 20, 2019, Art. no. 2453.

[45] J. Chen et al., "Registration and combined adjustment for the laser altimetry data and high-resolution optical stereo images of the GF-7 satellite," *Remote Sens.*, vol. 14, no. 7, 2022, Art. no. 1666.

[46] G. Li, X. Tang, C. Zhang, X. Gao, and J. Chen, "Multi-criteria constraint algorithm for selecting ICESat/GLAS data as elevation control points," *J. Remote Sens.*, vol. 21, no. 1, pp. 96–104, 2017.

[47] L. I. Guoyuan et al., "Processing and preliminary accuracy validation of the GF-7 satellite laser altimetry data," *Acta Geodaetica et Cartographica Sinica*, vol. 50, no. 10, 2021, Art. no. 1338.

[48] H. Hirschmuller, "Stereo processing by semiglobal matching and mutual information," *IEEE Trans. Pattern Anal. Mach. Intell.*, vol. 30, no. 2, pp. 328–341, Feb. 2008.

[49] X. Zhu, X. Tang, G. Zhang, B. Liu, and W. Hu, "Accuracy comparison and assessment of DSM derived from GFDM satellite and GF-7 satellite imagery," *Remote Sens.*, vol. 13, no. 23, 2021, Art. no. 4791.

[50] O. Sass, "Determination of the internal structure of alpine talus deposits using different geophysical methods (Lechtaler Alps, Austria)," *Geomorphology*, vol. 80, no. 1, pp. 45–58, 2006.

[51] J. Wu, C. Ma, W. Yang, L. Lyu, and L. Miao, "Recent expansion of talus slopes in the Northern Taihang Mountain Range, China: An example from the Xiaowutai Region," *Landslides*, vol. 18, no. 9, pp. 3027–3040, 2021.

[52] H. Hendrickx, L. De Sloover, C. Stal, R. Delaloye, J. Nyssen, and A. Frankl, "Talus slope geomorphology investigated at multiple time scales from high-resolution topographic surveys and historical aerial photographs (Sanetsch Pass, Switzerland)," *Earth Surf. Processes Landforms*, vol. 45, no. 14, pp. 3653–3669, 2020.

[53] S. Kaushik, T. Singh, A. Bhardwaj, P. K. Joshi, and A. J. Dietz, "Automated delineation of supraglacial debris cover using deep learning and multisource remote sensing data," *Remote Sens.*, vol. 14, no. 6, 2022, Art. no. 1352.

[54] F. Qing, Y. Zhao, X. Meng, X. Su, T. Qi, and D. Yue, "Application of machine learning to debris flow susceptibility mapping along the China–Pakistan Karakoram highway," *Remote Sens.*, vol. 12, no. 18, 2020, Art. no. 2933.

[55] Z. Zhang et al., "Deformation feature analysis of Qinghai–Tibet railway using TerraSAR-X and Sentinel-1A time-series interferometry," *IEEE J. Sel. Topics Appl. Earth Observ. Remote Sens.*, vol. 12, no. 12, pp. 5199–5212, Dec. 2019.

[56] P. Ma and H. Lin, "Robust detection of single and double persistent scatterers in urban built environments," *IEEE Trans. Geosci. Remote Sens.*, vol. 54, no. 4, pp. 2124–2139, Apr. 2016.

[57] RGIK, "Optional kinematic attribute in standardized rock glacier inventories (version 3.0.1). IPA action group rock glacier inventories and kinematics," 2022. [Online]. Available: https://bigweb.unifr.ch/Science/Geosciences/Geomorphology/Pub/Website/IPA/CurrentVersion/Current_KinematicalAttribute.pdf

[58] N. Short and R. Fraser, "Comparison of RADARSAT-2 and sentinel-1 DInSAR displacements over upland ice-wedge polygonal terrain, banks island, northwest territories, Canada," Geomatics Canada, Tech. Rep. Open File 73, 2023, p. 22, doi: 10.4095/331683.

[59] S. Gernhardt and R. Bamler, "Deformation monitoring of single buildings using meter-resolution SAR data in PSI," *ISPRS J. Photogrammetry Remote Sens.*, vol. 73, pp. 68–79, 2012.

[60] R. Bamler, M. Eineder, N. Adam, X. Zhu, and S. Gernhardt, "Interferometric potential of high resolution spaceborne SAR," *Photogrammetrie Fernerkundung Geoinformation*, vol. 2009, pp. 407–419, 2009.

[61] F. Bearzot et al., "Kinematics of an Alpine rock glacier from multitemporal UAV surveys and GNSS data," *Geomorphology*, vol. 402, 2022, Art. no. 108116.

[62] Y. Roa et al., "First assessment of the interferometric capabilities of SAOCOM-1A: New results over the Domuyo Volcano, Neuquén Argentina," *J. South Amer. Earth Sci.*, vol. 106, 2021, Art. no. 102882.

[63] T. Li, X. Tang, X. Zhou, X. Zhang, S. Li, and X. Gao, "Deformation products of lutan-1(Lt-1) sar satellite constellation for geohazard monitoring," in *Proc. IEEE Int. Geosci. Remote Sens. Symp.*, 2022, pp. 7543–7546.

[64] J. Buckel et al., "Rock glacier characteristics under semiarid climate conditions in the Western Nyainqêntanglha Range, Tibetan Plateau," *J. Geophysical Res.: Earth Surf.*, vol. 127, no. 1, 2022, Art. no. e2021JF006256.

[65] K. Senderak, M. Kondracka, and B. Gądek, "Processes controlling the development of talus slopes in SW Spitsbergen: The role of deglaciation and periglacial conditions," *Land Degradation Develop.*, vol. 32, no. 1, pp. 208–223, 2020.

Xuefei Zhang received B.Sc. degree in geoscience information system from Hebei GEO University, Hebei, China, in 2014, the M.Sc. degree in surveying and mapping from the China University of Geosciences, Beijing, China, in 2017, the Ph.D. degree in geographic information system from Aerospace Information Research Institute, Chinese Academy of Sciences, Beijing, in 2020.

From 2020 to 2022, he was engaged in postdoctoral research with the Institute of Tibetan Plateau Research, Chinese Academy of Sciences. He is currently an Assistant Research Fellow with the Land Satellite Remote Sensing Application Center, Ministry of Natural Resources, Beijing. His research interests include synthetic aperture radar (SAR) interferometric technique, time-series interferometric SAR, and their applications on permafrost, periglacial landforms.

Min Feng received the B.S. degree in physical geography, and the M.S. and Ph.D. degrees in cartography and geographic information system from Lanzhou University, Lanzhou, China, in 2002, 2005, and 2008, respectively.

He is currently a Professor with the Institute of Tibetan Plateau Research, Chinese Academy of Sciences (CAS), Beijing, China. He worked with the University of Maryland and the Institute of Geographic Sciences and Natural Resources Research, CAS after completing the Ph.D. degree. He was also a Senior Researcher with the Global Land Cover Facility (GLCF) and a Visiting Scholar with the UNEP Sioux Falls Center. He was appointed as a Geospatial Consultant to the World Bank. His research interests include remote sensing big data, land cover applications of remote sensing in global forest, and water mapping.

Tao Li received the B.Eng. degree in photogrammetry and remote sensing from the Shandong University of Science and Technology, Shandong, China, in 2009, and the Ph.D. degree in photogrammetry and remote sensing from the Southwest Jiaotong University, Chengdu, China, in 2014.

He is currently a Research Associate with the Land Satellite Remote Sensing Application Center, Ministry of Natural Resources, Beijing, China. He is also the Assistant Chief Engineer of the LuTan-1 SAR satellite application system. His current research interests include the SAR satellite argumentation, DSM generation using InSAR technology, deformation monitoring using DInSAR and MTInSAR technology.

Jiyi Chen received the B.S. degree in Geodesy and Geomatics from Wuhan University, Wuhan, China, in 2012, and the M.S. degree in photogrammetry and remote sensing from Chinese Academy of Surveying and Mapping, Beijing, China, in 2015.

He is currenlty an Assistant Researcher with the Land Satellite Remote Sensing Application Center, Ministry of Natural Resources, Beijing, China. His research interests include data processing and application of satellite laser altimetry, photogrammetry, and remote sensing.

Decai Jiang received the Bachelor of Engineering degree in surveying and mapping engineering from the China University of Mining and Technology, Jiangsu, China, in 2014, the Master of Engineering in photogrammetry and remote sensing from the Chinese Academic of Surveying and Mapping, Beijing, China, in 2017. Since 2020, he has been working toward the Ph.D. degree with the Northwest Institute of Eco-Environment and Resources, Chinese Academy of Sciences, Lanzhou, China.

His research interests include deep learning neural networks and their applications on identification of permafrost, periglacial landforms.

Jinhao Xu received the bachelor's and master's degrees in geoscience information system from Northwest University, Xi'an, China, in 2017 and 2020, respectively. In 2023, he received the Ph.D. degree in geoscience information system from the Institute of Tibetan Plateau Research, Chinese Academy of Sciences, Beijing, China.

He is currently engaged in postdoctoral research with the Institute of Tibetan Plateau Research, Chinese Academy of Sciences, Beijing. His main research interests include deep learning and remote sensing of periglacial landforms.

Dezhao Yan received B.Eng. degree in geological engineering from Henan Polytechnic University, Henan, China, in 2017, and the M.Sc. degree in geoscience information system from the China University of Geosciences, Beijing, China, in 2020. From 2020 to 2024, he studied as a doctor candidate in geoscience information system with the Institute of Tibetan Plateau Research, Chinese Academy of Sciences, Beijing.

His research interests include simulation of permafrost distribution, and research on periglacial geomorphology based on machine learning.

Xiaoqing Zhou received the Ph.D. degree in geodesy and surveying engineering from Wuhan University, Wuhan, China, in 2016.

He is currently a Research Fellow with the Land Satellite Remote Sensing Application Center, Ministry of Natural Resources, Beijing, China. His research interests include the fields of satellite remote sensing applications, and geodesy.

Xiang Zhang received the B.S. degree in survey and mapping engineering, the M.S. degree in geodesy and surveying engineering, and the Ph.D. degree in photogrammetry and remote sensing from the School of Environment Science and Spatial Informatics, China University of Mining and Technology, Xuzhou, China, in 2010, 2013, and 2016, respectively.

He is currently an Associate Researcher with the Land Satellite Remote Sensing Application Center, Ministry of Natural Resources, Beijing, China. His research interests include the fields of DEM reconstruction and deformation monitoring with the InSAR technique, soil and vegetation parameter retrieval using multisensor SAR data and SAR satellite system specification and simulation analysis.

Jing Lu received the master's degree in business administration from Beijing Normal University, Beijing, China, in 2013.

She is currently an Associate Researcher with the Land Satellite Remote Sensing Application Center, Ministry of Natural Resources, Beijing, China. Her main research interests are radar data processing parameter testing, as well as innovation platform management.